Journal of Power Sources 364 (2017) 410–419

Contents lists available at ScienceDirect

Journal of Power Sources

journal homepage: www.elsevier.com/locate/jpowsour

$Li_{14}P_2O_3N_6$ and Li_7PN_4: Computational study of two nitrogen rich crystalline LiPON electrolyte materials

Ahmad Al-Qawasmeh, N.A.W. Holzwarth*

Department of Physics, Wake Forest University, Winston-Salem, NC 27109-7507, USA

HIGHLIGHTS

- First principles simulations of $Li_{14}P_2O_3N_6$ and Li_7PN_4 electrolytes.
- Simulations predict stable electrolyte/Li interfaces for both materials.
- Predict Li ion migration activation energies comparable to other good electrolytes.

ARTICLE INFO

Article history:
Received 20 June 2017
Received in revised form
26 July 2017
Accepted 7 August 2017

Keywords:
Solid electrolytes
Li ion batteries
First principles calculations

ABSTRACT

Two lithium oxonitridophosphate materials are computationally examined and found to be promising solid electrolytes for possible use in all solid-state batteries having metallic Li anodes – $Li_{14}P_2O_3N_6$ and Li_7PN_4. The first principles simulations are in good agreement with the structural analyses reported in the literature for these materials and the computed total energies indicate that both materials are stable with respect to decomposition into binary and ternary products. The computational results suggest that both materials are likely to form metastable interfaces with Li metal. The simulations also find both materials to have Li ion migration activation energies comparable or smaller than those of related Li ion electrolyte materials. Specifically, for Li_7PN_4, the experimentally measured activation energy can be explained by the migration of a Li ion vacancy stabilized by a small number of O^{2-} ions substituting for N^{3-} ions. For $Li_{14}P_2O_3N_6$, the activation energy for Li ion migration has not yet been experimentally measured, but simulations predict it to be smaller than that measured for Li_7PN_4.

1. Introduction

Twenty-five years after the pioneering work at Oak Ridge National Laboratory on LiPON solid electrolytes [1–9], new crystalline lithium oxonitridophosphate materials continue to be discovered. While the technologically viable LiPON electrolyte is disordered [1], studies of compositionally related crystalline materials has provided valuable insight. LiPON materials have the stoichiometry $Li_xPO_yN_z$ with $x = 2y + 3z - 5$. The building blocks of these materials are the PO_uN_{4-u} tetrahedra which are often formed into dimers, trimers, infinite chains, or more complicated interconnections [10–12]. Recently, Baumann and Schnick [13] found an interesting new crystalline LiPON which has the stoichiometry $Li_{14}P_2O_3N_6$, formed with a trigonal arrangement of isolated tetrahedral $(PON_3)^{6-}$ ions and stabilized by isolated O^{2-} ions. A related electrolyte, having the stoichiometry of Li_7PN_4 and based on a cubic arrangement of isolated tetrahedral $(PN_4)^{7-}$ ions, was previously synthesized and characterized by Schnick and Luecke [14,15]. These are two examples of nitrogen rich LiPON materials constructed from isolated oxonitridophosphate tetrahedra. In the present work, we report the results of our computational study of the bulk and interface structures and Li ion migration properties of both $Li_{14}P_2O_3N_6$ and Li_7PN_4. Results are compared with analogous studies of Li_3PO_4 [16–21].

2. Computational methods

The computational methods used in this work are based on density functional theory (DFT) [22,23], implemented by the projected augmented wave (PAW) [24] formalism. The PAW basis and projector functions were generated by the ATOMPAW [25] code and used in the QUANTUM ESPRESSO [26] package. Visualizations of the crystal structures were constructed using the *XCrySDEN* [27,28],

* Corresponding author.
E-mail address: natalie@wfu.edu (N.A.W. Holzwarth).

http://dx.doi.org/10.1016/j.jpowsour.2017.08.025
0378-7753/

VESTA [29] software packages.

The exchange correlation function is approximated using the local-density approximation (LDA) [30]. The choice of LDA functional was based on previous investigations [10,11,17,19,20,31] of similar materials which showed that the simulations are in good agreement with experiment, especially the fractional lattice parameters, the vibrational frequencies, and heats of formation. The simulated magnitudes of the lattice parameters, when systematically scaled by a factor of 1.02, are also in good agreement with experiment.

The calculations were well converged with plane wave expansions of the wave function including $|\mathbf{k}+\mathbf{G}|^2 \leq 64$ bohr^{-2}. The Brillouin zone integrals were evaluated volumes of 0.006 bohr^{-3} or smaller. Convergence tests showed that increasing the sampling volumes by a factor of 8 changed the total energy by less than 0.001 eV for 100 atom supercells.

The partial densities of states were calculated as described in previous work [20,32], using weighting factors determined from the charge within the augmentation spheres of each atom with radii $r_c^{\mathrm{Li}} = 1.6$, $r_c^{\mathrm{P}} = 1.7$, $r_c^{\mathrm{O}} = 1.2$, and $r_c^{\mathrm{N}} = 1.2$ in bohr units. The reported partial densities of states curves $\langle N^a(E)\rangle$ represent results averaged over the atomic sites of each type a. The Gaussian width used to evaluate the density of states was 0.01 eV.

Simulation of Li ion migration were performed at constant volume in supercells constructed from the optimized conventional cells. In modeling charged defects (Li ion vacancies or interstitials), the system was assumed to remain electrically insulating and a uniform background charge was added in order to evaluate the electrostatic interactions. The minimum energy path for Li ion migration was estimated using the "nudged elastic band" (NEB) method [33–35] as programmed in the QUANTUM ESPRESSO package, using 5 images between each metastable configuration. For each minimum energy path, the migration energy, E_m was determined as the energy difference between the lowest and highest energy of the path. The "formation energies" E_f for producing neutral defects in the form of vacancy-interstitial pairs were calculated within the same supercells. These energies are related to the experimentally measured ionic conductivity through an Arrhenius relationship of the form

$$\sigma = \frac{C}{T} e^{-E_A/kT}, \tag{1}$$

where C denotes a constant, T denotes the temperature in Kelvin, k denotes the Boltzmann constant, and E_A denotes the activation energy for ion migration. The activation energy E_A is related to the migration and formation energies according to [36].

$$E_m \leq E_A \leq E_m + \frac{1}{2}E_f. \tag{2}$$

In Eq. (2) the upper limit of E_A applies to the "intrinsic" case when ion migration is initiated by the creation of a pair of vacancy and interstitial ions with energy E_f by thermal activation in addition to the migration barrier E_m. The lower limit applies to the "extrinsic" case when a population of vacancy or interstitial ions is available in the sample so that the conduction depends only on the thermal activation due to the migration energy barriers characterized by E_m. Experimentally, sample preparation conditions presumably control the intrinsic versus extrinsic behaviors of the activation energy E_A. The static calculations cannot estimate the prefactor C, but calculations of E_m and E_f can provide the expected range of activation energies E_A according to Eq. (2).

Another important attribute of solid electrolytes is their interface properties, particularly their interfaces with metallic Li. These were modeled in supercells containing alternating slabs of electrolyte and Li metal. The supercells were constrained to the optimized lattice parameters of the bulk electrolyte in the directions parallel to the interface, while the lattice parameter along the interface normal direction was allowed to vary in order to minimize the energy of the simulation cell. This procedure finds many metastable configurations of the interface. For some of the simulations we made a more quantitative assessment of the interface stability, following the approach of Lepley et al. [21] who defined a quasi-intensive interface energy between materials a and b as

$$\gamma_{ab}(\Omega) = \frac{E(\Omega, A, n_a, n_b) - n_a E_a - n_b E_b}{2A}. \tag{3}$$

Here $E(\Omega, A, n_a, n_b)$ is the optimized total energy of the supercell containing the interface with n_a and n_b formula units of materials a and b. E_a and E_b denote the bulk energy per unit cell of materials a and b. Ω represents the particular configuration of the system. A denotes the area normal to the surface; because of the periodic boundary conditions, each supercell necessarily has two equal area interfaces. For our case, material a represents the electrolyte – $Li_{14}P_2O_3N_6$ or Li_7PN_4 – and material b represents metallic Li. In order to assess the strain introduced by the periodic boundary conditions, the supercells are prepared with fixed n_a with the ideal lattice constants of the electrolyte, and a series of calculations are performed with similar configurations but varying numbers n_b of metallic Li atoms. The set of calculations can then be fit to an equation which varies linearly with n_b in the form

$$\gamma_{ab}(\Omega, n_b) = \gamma_{ab}^{\lim}(\Omega) + n_b \sigma(\Omega). \tag{4}$$

Here $\sigma(\Omega)$ represents the strain of the metallic Li in the configuration Ω and $\gamma_{ab}^{\lim}(\Omega)$ represents the surface energy extrapolated to zero strain. For these systems, it is also interesting to reference the interface of the electrolyte with vacuum, for which Eq. (3) can be used with $n_b \equiv 0$.

3. Computational results

3.1. $Li_{14}P_2O_3N_6$

3.1.1. Structure of bulk $Li_{14}P_2O_3N_6$

Baumann and Schnick [13] reported the synthesis of $Li_{14}P_2O_3N_6$ by heating powders of $PO(NH_2)_3$ and $LiNH_2$ in a sealed silica glass ampoule for 24 h at a temperature of 550 deg. C. The resulting crystals were analyzed to have a trigonal structure characterized by the space group $P\bar{3}$ (No. 147 as listed in the International Table of Crystallography) [37]. Fig. 1 shows a ball and stick diagram of the structure from two different perspectives and Table 1 lists the calculated lattice parameters compared with experimental results. The scale factor of 1.02, used to correct the systematic LDA error on the magnitudes of the lattice constants, puts the simulated lattice constants within 0.1 Å of the experimental results. The simulated fractional coordinates for the P, O, and N sites are all within 0.01 of the experimental results. For the Li sites, the simulated fractional coordinates differ from the experimental values by a larger amount (0.06 or less). It is our experience [38] that it is common to find that X-ray analysis is less sensitive to the Li positions than to the positions of the other elements in the crystal which have larger X-ray cross sections due to their larger atomic numbers Z.

Simulations show that the trigonal symmetry is stabilized by the isolated O^{2-} ions located at 1b sites and the corresponding Li^+ ions located at 2c sites. In addition to its trigonal symmetry, the crystal structure features an interesting arrangement of pairs of PON_3 tetrahedra, forming c-axis planes of alternating O^{2-} and N^{3-} ions.

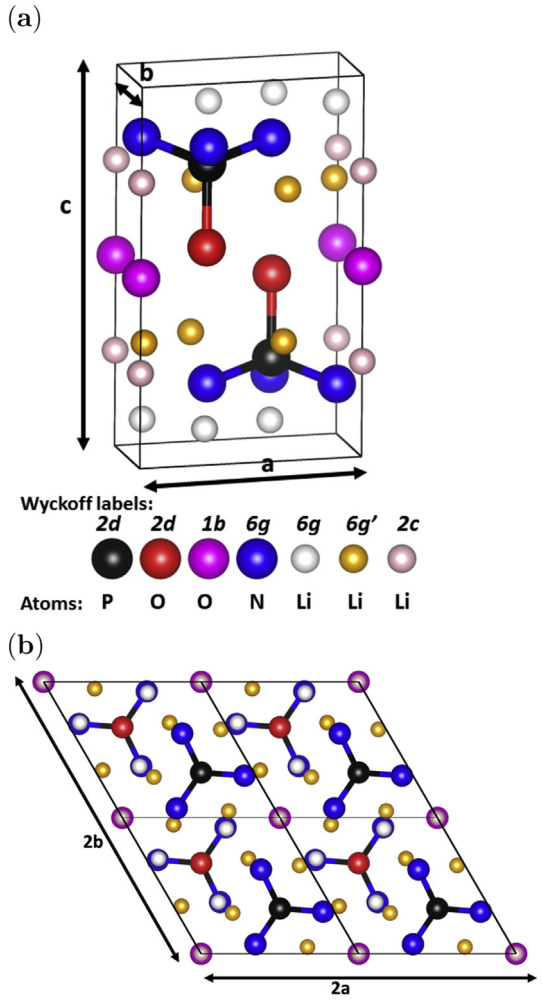

Fig. 1. (a) Ball and stick diagram of the $P\bar{3}$ structure of a unit cell of $Li_{14}P_2O_3N_6$, viewing the **c** -axis along the vertical direction, using the indicated ball conventions to distinguish the inequivalent sites, labeled according to their Wyckoff letters. (b) Projection of 4 unit cells of $Li_{14}P_2O_3N_6$ perpendicular to the **c** axis to show the trigonal symmetry.

Table 1
Optimized lattice parameters and fractional atomic positions of $Li_{14}P_2O_3N_6$ having the space group $P\bar{3}$ (#147) compared with experimental results reported in Ref. [13]. The simulated lattice parameters are multiplied by 1.02 factor to compensate for the underestimation of distances in the LDA approximation.

		Lattice constants (Å)	
		Simulation (this work)	Experiment (Ref. [13])
a		5.66	5.69
c		7.99	8.09
		Fractional coordinates Simulation (this work)	Experiment (Ref. [13])
Atom	Site	(x,y,z)	(x,y,z)
Li	6g	(0.08,0.70,0.91)	(0.05,0.64,0.91)
Li	6g′	(0.35, 0.30,0.41)	(0.29,0.29,0.41)
Li	2c	(0, 0, 0.75)	(0, 0, 0.77)
P	2d	$(\frac{1}{3},\frac{2}{3},0.23)$	$(\frac{1}{3},\frac{2}{3},0.24)$
O	2d	$(\frac{1}{3},\frac{2}{3},0.45)$	$(\frac{1}{3},\frac{2}{3},0.45)$
O	1b	$(0, 0,\frac{1}{2})$	$(0, 0,\frac{1}{2})$
N	6g	(0.07,0.69,0.17)	(0.06,0.69,0.17)

The arrangement of the isolated oxonitridophosphate tetrahedra is quite different from other crystalline LiPON materials of this type such as Li_7PN_4 [14,15] and $\beta-$ and $\gamma-$ Li_3PO_4 which was studied previously [18,39].

It is interesting to compare the electronic structure of $Li_{14}P_2O_3N_6$ with other oxonitridophophates composed of isolated tetrahedra and related materials. The corresponding partial densities of states are given in Fig. 2. The valence band states are characterized by the 2*p* states of O and N together with bonding combinations the P 3*s* and 3*p* states while the conduction bands are characterized by the corresponding antibonding states. The N 2*p* states dominate the top of the valence band for $Li_{14}P_2O_3N_6$. The O 2*p* contributions to $Li_{14}P_2O_3N_6$ are of two types. The occupied states associated with P-O bonds contribute to the bottom of the valence band, while the non-bonded O 2*p* states contribute to the middle of the valence band. Knowing that LDA calculations typically underestimate band gaps, we can safely conclude that the four materials are good insulators, having band gaps larger than 3 eV.

Related to the electronic structure is the stability of the compounds relative to decomposition. In order to thoroughly study the stability of this system, it would be helpful to construct a phase diagram such as achieved for $LiFePO_4$ by Ong et al. [40]. While this is beyond the purview of the present study, some information about the stability can determined by considering the energies of some possible chemical reactions. These can be roughly estimated from the calculated total energies, assuming that vibrational energies including zero point energies can be neglected. For example, we considered the following possible decomposition reaction.

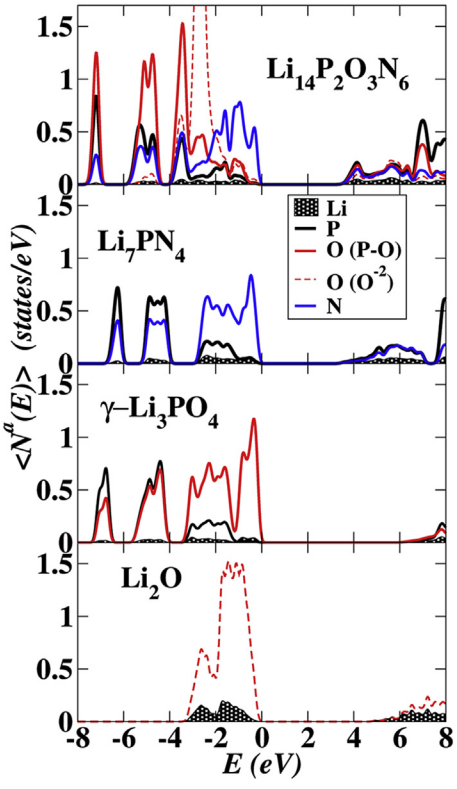

Fig. 2. Partial density of states plot for the LiPON materials $Li_{14}P_2O_3N_6$ and Li_7PN_4 in comparison with γ-Li_3PO_4 and Li_2O. Oxygen contributions from isolated O^{2-} ions and from oxygens associated with P–O bonds are distinguished with dashed and full red lines, respectively. In each plot, $E = 0$ is aligned at the top of the valence band. (For interpretation of the references to colour in this figure legend, the reader is referred to the web version of this article.)

$$Li_{14}P_2O_3N_6 \rightarrow 3Li_2O + 2Li_3N + 2LiPN_2 - 2.9\ eV. \quad (5)$$

The negative energy on the right side of the equation indicates that $Li_{14}P_2O_3N_6$ is stable with respect to decomposition into these binary and ternary products. In anticipation of the study of interfaces of this electrolyte with Li metal, we also considered the energy associated with reaction with Li metal as follows.

$$Li_{14}P_2O_3N_6 + 16Li \rightarrow 3Li_2O + 6Li_3N + 2Li_3P + 3.1\ eV. \quad (6)$$

This reaction is exothermic, suggesting that under equilibrium conditions the interfaces would react with Li metal. However the exothermic energy is considerably smaller than 13.3 eV estimated for the analogous reaction of Li_3PO_4 and Li metal [21].

3.1.2. Li ion migration mechanisms in $Li_{14}P_2O_3N_6$

Li ion migration in $Li_{14}P_2O_3N_6$ was investigated using supercells based on $2 \times 2 \times 1$ multiples of the unit cell. The energies of point defects were estimated from constant volume optimization of each structure containing a Li ion vacancy or interstitial and compensating uniform charge density within the supercell. Table 2 summarizes the 3 inequivalent vacancy energies relative to the g' site vacancy and 2 inequivalent interstitial energies relative to the I site interstitial. The placements of these defect sites are illustrated in Fig. 3(a) and (c) in an orthorhombic construction of the hexagonal unit cell.

In order to study likely migration pathways, using the NEB method [33–35], we considered a range of near neighbor hops between defect sites as summarized in Table 3. In this table, the distances d between defect sites are estimated from the perfect crystal configurations. The results show that ΔE, the calculated energy variation within each trajectory between pairs of metastable configurations, is sensitive both to the distance d and to the local environment of the trajectory.

Considering Li ion vacancy migration, the large range of the relative energies of the unique vacancy configurations listed in Table 2 suggests that the energetically favorable vacancy migration processes are confined to hops between vacancies on equivalent sites. Table 3 lists the unique hops likely to contribute to Li ion migration in this material. These include several migration pathways between vacancies on g' sites and several pathways between vacancies on g sites. Geometric considerations suggest that c site vacancies are less likely to be involved in effective Li ion migration processes. The corresponding energy path diagrams are given in Fig. 3(b) for the vacancy mechanisms and in Fig. 3(d) for mechanisms actively involving interstitial sites.

The visualization of the trajectories shown in Fig. 3(a) shows that the vacancy migration processes involving sites of type g' take place near planes of the crystal that include oxygen ions. The path $g'_1 \rightarrow g'_2 \rightarrow g'_3 \rightarrow g'_4 \rightarrow g'_5$ is characterized by two unique hops. The hop $g'_1 \rightarrow g'_2$ has a relatively low energy variation of $\Delta E = 0.3$ eV, while the hop $g'_2 \rightarrow g'_3$ has a more complicated trajectory with a net energy variation of $\Delta E = 0.4$ eV. Examination of details of the trajectory shows that substantial rearrangement of the neighboring ions in the vicinity of a metastable interstitial configuration. The rearrangement lowers the energy of the configuration below that of the pure g' vacancy and thus increases the overall migration energy for the trajectory to $E_m = 0.4$ eV. The path $g'_6 \rightarrow g'_7 \rightarrow g'_8 \rightarrow g'_9 \rightarrow g'_{10}$ is characterized by one unique hop $g'_6 \rightarrow g'_7$ which is identical to the hop $g'_1 \rightarrow g'_2$ having an energy variation of $\Delta E = 0.3$ eV resulting in the net migration barrier of $E_m = 0.3$ eV which is the lowest migration barrier found for this material in this study.

Vacancy migration processes involving sites of type g take place near planes of the crystal that include nitrogen ions. The path $g_6 \rightarrow g_7 \rightarrow g_8 \rightarrow g_9$ involves motion along the hexagonal **a** axis with two unique hops. The hop $g_6 \rightarrow g_7$ has an energy variation of $\Delta E = 0.3$ eV and the longer distance hop $g_7 \rightarrow g_8$ has an energy variation of $\Delta E = 1.6$ eV, resulting in the net migration barrier of $E_m = 1.6$ eV for this path. The path $g_1 \rightarrow g_2 \rightarrow g_3 \rightarrow g_4 \rightarrow g_5$ also involves net motion along the hexagonal **a** axis with two unique hops. The hop $g_1 \rightarrow g_2$ is identical to the hop $g_6 \rightarrow g_7$, while the hop $g_2 \rightarrow g_3$ has a component along the **c** axis having an energy variation of $\Delta E = 0.6$ eV. The overall path which has a net motion along the hexagonal **a** axis in alternating proximity to two nearby nitrogen planes of the crystal, has a net migration energy of $E_m = 0.6$ eV.

Li ion migration mechanisms involving interstitial sites were also consider as visualized in Fig. 3(c). A pure interstitial path was found in the proximity to two neighboring nitrogen planes, involving interstitial Li ions hopping 3.2 Å between type I and II sites. This path requires the Li ion to migrate through a region containing significant numbers of host lattice Li ions of type g. The simulations find significant distortion of the host lattice ions and the resulting energy variation along the path is very large – $\Delta E > 2$ eV, suggesting that the pure interstitial mechanism is unlikely to contribute to the migration processes. On the other hand, a related kickout process, involving the same interstitial sites in concerted motion with nearby g site host lattice Li ions,as illustrated in Fig. 3(c), was found to have an energy variation of $\Delta E = 0.6$ eV as shown in the energy path diagram of Fig. 3(d).

In order for Li ion migration to occur within a well-ordered crystalline material, it is necessary to take into account the "formation" energy E_f of vacancy-interstitial pairs of defects. The possible values of E_f for this material were estimated by optimizing defect pair geometries within the supercell, spanning the possibilities with interstitials of each type (I and II) and near-neighbor vacancies of the types g', g, and c. For the pairs I-c and II-c, the formation energy was found to be relatively large – $E_f \approx 1.0$ eV. For the pairs I-g and II-g, the formation energy was found to be very large – $E_f > 1.6$ eV. However, for the pairs of type I-g', some smaller formation energies were found, with the minimum value of $E_f = 0.3$ eV, involving nearest neighbor I and g' sites. Formation energies of type II-g' were found be $E_f > 1.0$ eV.

From the analysis of E_m and E_f for this material, vacancy mechanism of diffusion near the oxygen planes with g' sites was found to be the most favorable with a migration energy $E_m = 0.3$ eV and the minimum formation energy for this material was found to be $E_f = 0.3$ eV. From these results the simulated activation energy can be estimated from Eq. (2) to be $0.3 \leq E_A \leq 0.4$ eV.

3.1.3. $Li_{14}P_2O_3N_6$/Li interfaces

From the structure of $Li_{14}P_2O_3N_6$ shown in Fig. 1, a likely cleavage seems to be normal to the **c** axis between two planes

Table 2
Distinct vacancy and interstitial Li ion sites within the unit cell of $Li_{14}P_2O_3N_6$ and their relative energies estimated from $2 \times 2 \times 1$ supercell optimizations. The reference energies were chosen as the g' site for the vacancy defects and the I site for the interstitial defects.

Vacancies	
Multiplicity and Wyckoff Label	Relative Energy (eV)
4g'	0.00
4g	0.95
2c	0.41
Interstitials	
Fractional Coordinates	Relative Energy (eV)
$I \equiv (\frac{1}{3}, \frac{2}{3}, 0.73)$ (2d)	0.00
$II \equiv (0, 0, 0)$ (1a)	0.22

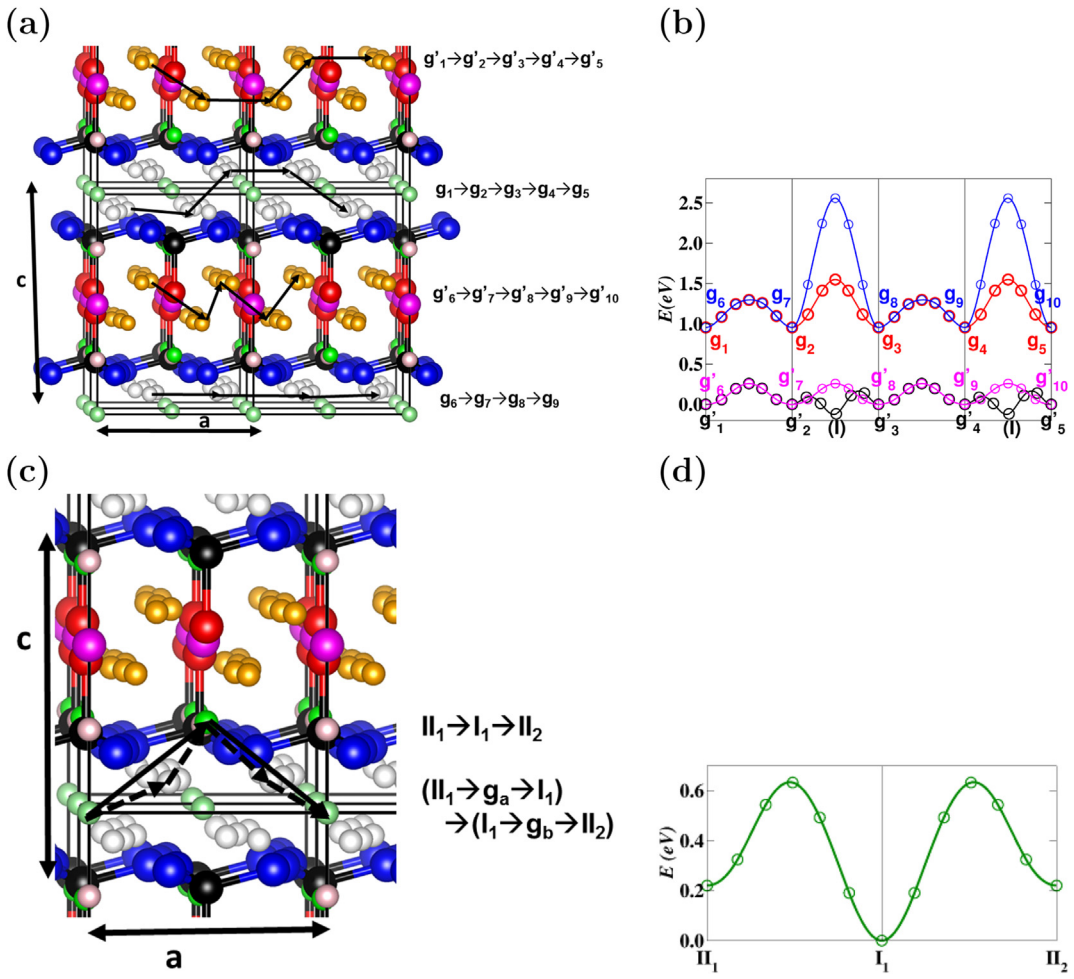

Fig. 3. Panels (a) and (c) show ball and stick models of several supercells of $Li_{14}P_2O_3N_6$ using the same ball conventions as in Fig. 1 with the addition of type *I* and *II* interstitial sites shown in bright and pale green, respectively. The **a** and **c** axes are indicated in the diagrams while the third axis of the diagram is perpendicular to the other two, specifically constructed in the **a** + 2**b** direction. Panels (b) and (d) show energy path diagrams from NEB simulations of Li ion migration between metastable vacancy or interstitial configurations indicated by the vertical lines. Panel (a) shows 4 possible vacancy migration paths and panel (b) shows the corresponding energy path diagram, choosing the zero of energy at the g' vacancy configuration. Panel (c) shows possible interstitial (full arrows) and kickout (dashed arrows) mechanisms for Li ion migration and panel (d) shows the correspondoing energy path diagram, choosing the zero of energy at the *I* interstitial configuration. (For interpretation of the references to colour in this figure legend, the reader is referred to the web version of this article.)

Table 3
Summary of Li ion migration steps in $Li_{14}PO_3N_6$ using site labels are given in Figs. 3 (a) and (c). The hop distance d is based on ideal lattices before defect optimization. The energy range within each hop is given as ΔE.

Type	Sites	d (Å)	ΔE (eV)
Vacancy	$g'_1 \rightarrow g'_2$, $g'_6 \rightarrow g'_7$	2.3	0.3
Vacancy	$g'_2 \rightarrow g'_3$	2.6	0.4
Vacancy	$g_1 \rightarrow g_2$, $g_6 \rightarrow g_7$	2.6	0.3
Vacancy	$g_2 \rightarrow g_3$	2.4	0.6
Vacancy	$g_7 \rightarrow g_8$	3.3	1.6
Interstitial	$II_1 \rightarrow I_1$	3.2	> 2.0
Kickout	$II_1 \rightarrow g_a \rightarrow I_1$	2.0 + 2.0	0.6

containing N. Using Eq. (3) with $n_b = 0$, we find $\gamma(Li_{14}P_2O_3N_6[\mathbf{c}]/\text{vac}) = 0.07$ eV/Å^2. The result is insensitive to the number of electrolyte layers; converging within 0.001 eV/Å^2 even for a single layer. All other vacuum cleavages for this material were found to have a larger surface energy by at least 50%. The surface energy for this system is similar to that of γ-Li_3PO_4, which was reported by Lepley et al. [21] to be 0.04 eV/Å^2 and 0.07 eV/Å^2 for surface normals along the **a** and **b** axes, respectively.

We prepared two series of configurations of interfaces of $Li_{14}P_2O_3N_6[\mathbf{c}]$ with Li as shown in Fig. 4(a) and (b) and the corresponding plots of the surface energy versus the number of metallic lithium atoms n_b are evaluated according to Eq. (4) as plotted in Fig. 4(c). Interface configurations Ω_1 and Ω_2 have approximately the same density of the Li atoms per unit volume 0.05–0.06 atoms/Å^3, close to the density of bulk Li. The estimated strains of the two configurations are $\sigma(\Omega_1) = 0.0004$ eV/Å^2 and $\sigma(\Omega_2) = 0.0014$ eV/Å^2, consistent with the notion that the more regular structure of configuration Ω_1 produces smaller strain. The strain corrected interface energy, γ_{ab}^{lim}, for the two configurations is found to be approximately 0.05 eV/Å^2. This value is similar to the corresponding values of 0.03–0.04 eV/Å^2 reported by Lepley et al. [21] for interfaces of β- or γ- Li_3PO_4 with Li metal.

The partial densities of states for the interface 4(a) with $n_b = 36$ are shown in Fig. 4(d). Even though the supercell contains only one formula unit of the electrolyte, the partial densities of states for the interior of the electrolyte is very similar to that of the bulk structure of $Li_{14}P_2O_3N_6$ shown in Fig. 2. The metallic Li states are physically separated from the electrolyte, but energetically overlap with the top of the $Li_{14}P_2O_3N_6$ valence band by approximately 1 eV. The

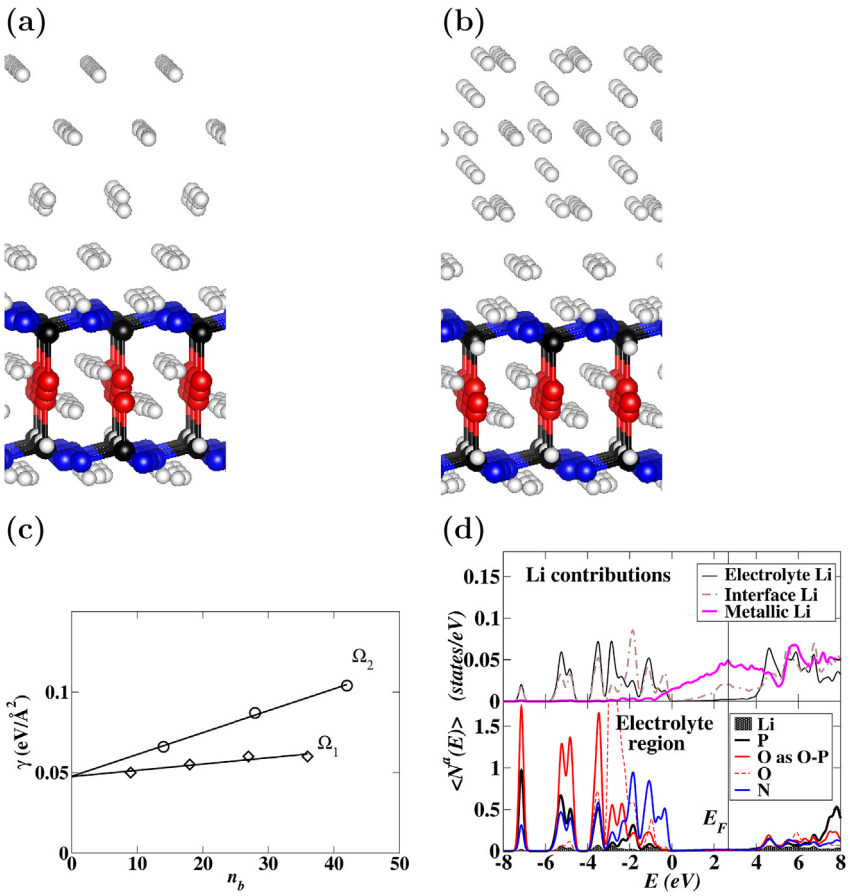

Fig. 4. Ball and stick models of interfaces of $Li_{14}P_2O_3N_6$[**c**]/Li from viewpoints similar to that given in Fig. 3 using simplified ball conventions with light gray, black, red, and blue balls representing Li, P, O, and N sites, respectively. Li configurations Ω_1 and Ω_2 are shown in panels (a) and (b), respectively. Panel (c) plots the interface energy for the two configuragions as a function of n_b Li metal atoms, evaluated according to Eq. (4). Panel (d) presents the partial densities of states of configuration Ω_1 with 36 metallic Li atoms in the supercell. The zero of energy for the $\langle N^\alpha(E)\rangle$ plots is taken as the top of the valence band of the bulk electrolyte. The bottom portion of the plot shows the five contributions to partial densities of states from the interior of the electrolyte in the supercell, while the upper portion compares the partial densities of states of the three types of Li using an expanded intensity scale. (For interpretation of the references to colour in this figure legend, the reader is referred to the web version of this article.)

partial densities of states associated with the Li ions at the interface of the electrolyte and the metallic Li, show that they have more electronic charge than the Li^+ ions in the interior of the electrolyte. The "Electrolyte Li" curve in the top portion of the plot 4(d) is the same as the "Li" curve in lower portion of the plot representing ionic Li within the interior of the electrolyte. Also shown in the top portion of the plot 4(d) are the "Interface Li" contributions corresponding to Li sites nearest the electrolyte and the "Metallic Li" contributions corresponding to the interior of the metallic Li region of the supercell.

3.2. Li_7PN_4

3.2.1. Structure of the bulk Li_7PN_4

Li_7PN_4 was synthesized by Schnick and Luecke [14,15] by sealing Li_3N and P_3N_5 under a nitrogen atmosphere in a quartz tube and heating to 620 deg C for one hour. The resulting crystals were analyzed to have a cubic structure with the space group $P\bar{4}3n$ (No. 218) with 8 formula units (96 atoms) in each unit cell. A ball and stick diagram of the unit cell is shown in Fig. 5. Table 4 lists the lattice parameters from the simulation in comparison with the experimental results. The comparison is quite good. The LDA corrected simulated lattice constants agree with experiment within 0.02 Å, and the fractional coordinates including the Li sites agree within 0.01.

The partial densities of states for Li_7PN_4 was shown in Fig. 2 in comparison with the related materials of this study. The similarity of the electronic structure with Li_3PO_4 is evident from these plots, while Li_7PN_4 has a smaller valence band width and a smaller gap between the conduction and valence bands compared with Li_3PO_4.

With a view toward considering a limited study of the stability of this system, from the electronic structure results, we can consider the following decomposition reactionr:

$$Li_7PN_4 \rightarrow 2Li_3N + LiPN_2 - 2.9\ \text{eV}. \quad (7)$$

The negative energy on the right side of the equation indicates that Li_7PN_4 is stable with respect to decomposition into these binary and ternary products. We can also consider interaction with metallic Li.

$$Li_7PN_4 + 8Li \rightarrow 4Li_3N + Li_3P + 0.2\ \text{eV}. \quad (8)$$

This reaction is exothermic suggesting that under equilibrium conditions the interfaces would react with Li metal. However the exothermic energy in this case is very small compared with the corresponding reaction energies of other LiPON electrolytes as discussed above.

3.2.2. Li ion migration mechanisms in Li_7PN_4

We also considered Li ion migration mechanisms in Li_7PN_4. The

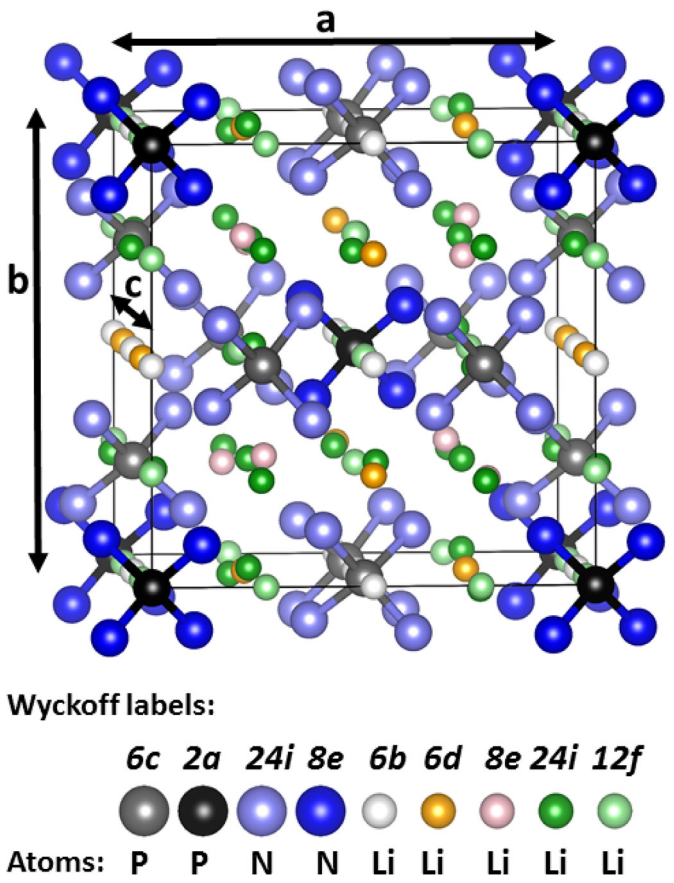

Fig. 5. Ball and stick diagram of the $P\bar{4}3n$ structure of a unit cell of Li_7PN_4, using the indicated ball conventions to distinguish the inequivalent sites; labeled with their Wyckoff letters. The axes **a**, **b** and **c** are equivalent.

Table 4
Optimized lattice parameters and fractional atomic positions of Li_7PN_4 having the space group $P\bar{4}3n$ (♯ 218) compared with experimental results reported in Ref. [14]. The simulated lattice parameters are multiplied by 1.02 factor to compensate for the underestimation of distances of LDA approximation.

		Lattice constant (Å)	
		Simulation (this work)	Experiment (Ref. [14])
a		9.34	9.36
		Fractional coordinates	
		Simulation (this work)	Experiment (Ref. [14])
Atom	Site	(x,y,z)	(x,y,z)
Li	6*b*	$(0,\frac{1}{2},\frac{1}{2})$	$(0,\frac{1}{2},\frac{1}{2})$
Li	6*d*	$(\frac{1}{4},0,\frac{1}{2})$	$(\frac{1}{4},0,\frac{1}{2})$
Li	8*e*	(0.23, 0.23,0.23)	(0.22,0.22,0.22)
Li	12*f*	(0.26,0,0)	(0.26,0,0)
Li	24*i*	(0.25,0.24,0.98)	(0.25,0.24,0.97)
P	6*c*	$(\frac{1}{2},0,\frac{1}{4})$	$(\frac{1}{2},0,\frac{1}{4})$
P	2*a*	(0,0,0)	(0,0,0)
N	24*i*	(0.35,0.39,0.10)	(0.35,0.38,0.10)
N	8*e*	(0.10,0.10,0.10)	(0.10,0.10,0.10)

simulations were performed using the unit cell since it is quite large, containing 96 atoms. Vacancies were simulated by removing one Li^+ ion and adding a compensating uniform charge of $+e$ within the simulation cell. There are five distinct vacancy sites and the corresponding relative vacancy energies are given in Table 5. Interstitials were simulated by adding one Li^+ ion and adding a compensating uniform charge of $-e$ within the simulation cell. Two distinct low energy interstitial sites were found and these are also listed in Table 5, including their Wyckoff site label.

Table 5
Distinct vacancy and interstitial Li ion sites in Li_7PN_4 and their relative energies. The *f* vacancy site is chosen as the reference for the vacancy sites, and the *I* interstitial type is chosen as the reference for the interstitial sites.

Vacancies	
Multiplicity and Wyckoff Label	Relative Energy (eV)
6*b*	0.15
6*d*	0.25
8*e*	0.00
12*f*	0.00
24*i*	0.10
Interstitials	
Fractional Coordinates	Relative Energy (eV)
I≡(0.36, 0.85, 0.38) (24*i*)	0.00
II≡(0.36, 0.36, 0.36) (8*e*)	0.32

For simulating Li ion vacancy migration, it was determined that the paths with the shortest hops are along one of the equivalent crystallographic axes. For example, in Fig. 5, three distinct paths along the **c**-axis can be visualized. The corresponding energies along the migration path as computed with the NEB approach are illustrated in Fig. 6(a). From these diagrams, it is apparent that the path $i \to e \to i \to e \to i$ has the smallest migration energy with $E_m = 0.3$ eV. The simulations also show that the smallest "formation" energy for an interstitial-vacancy pair $E_f = 1.9$ eV, corresponding to a type *I* interstitial paired with a all types of nearby vacancies within 5 Å distance from the interstitial. From these results, the simulated activation energy from Eq. (2) can be estimated to be $0.3 \le E_A \le 1.3$ eV. On the other hand, the experimental

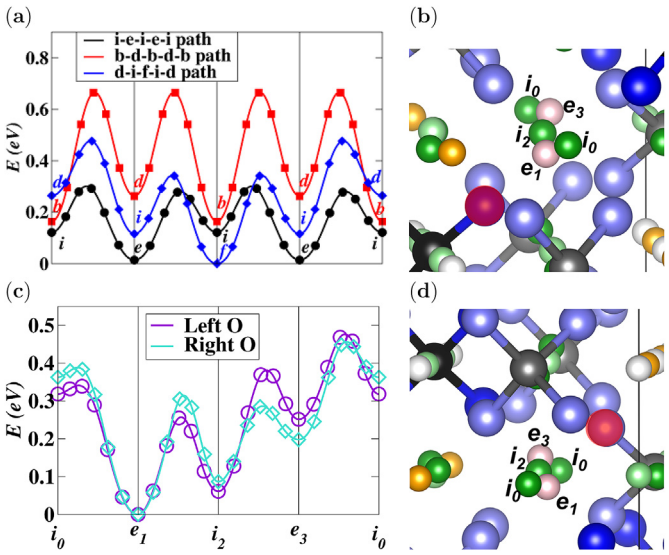

Fig. 6. (a) Energy path diagram for Li ion vacancy migration in Li_7PN_4, showing three distinct trajectories between metastable vacancy configurations indicated with the vertical lines and corresponding to the indicated Wyckoff labels; the zero of energy is taken as a Li ion vacancy at a *f* site. (c) Energy path diagram for Li ion vacancy migration in Li_7PN_4 in the vicinity of an O ion substituting for N; the zero of energy is taken to be the lowest energy of the path (at the e_1 site Li ion vacancy). Panels (b) and (d) show sections of the unit cell of Li_7PN_4 as shown in Fig. 5 in the vicinity of Li sites $i \to e \ldots$. These sections each have a substituted O ion represented by a red ball on the "Left" and "Right" sides of the path in panels (b) and (d), respectively. (For interpretation of the references to colour in this figure legend, the reader is referred to the web version of this article.)

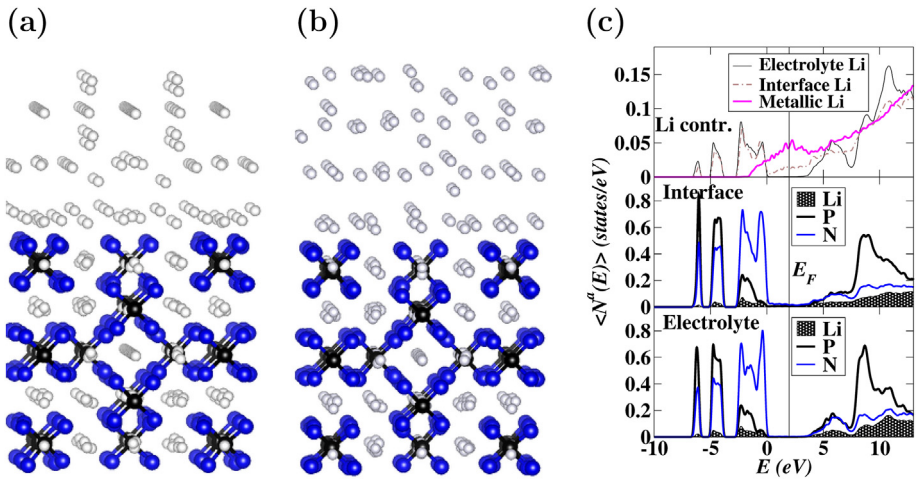

Fig. 7. Panels (a) and (b) show ball and stick models of Li_7PN_4 interfaced with metallic Li in two distinct configurations. The ball conventions have been simplified so that light gray, black, and blue balls represent Li, P, and N sites, respectively. Panel (c) shows partial densities of states corresponding to configuration (b), with separate $\langle N^a(E)\rangle$ contributions for the interior of the electrolyte, the interface region, and the contributions from the three types of Li sites using an expanded intensity scale. The zero of energy for the plots is taken as the top of the valence band of the bulk electrolyte. (For interpretation of the references to colour in this figure legend, the reader is referred to the web version of this article.)

impedance measurements find the activation energy for ionic conductivity to be $E_A = 0.48$ eV [15], suggesting that the experimental samples have a significant source of Li ion vacancies besides those available from thermal activation.

We reasoned that a possible source of Li ion vacancies in the experimental samples might be due to the presence of O ions replacing a small number N ions within the crystal. Since O^{2-} ions can be compensated with 2 Li^+ ions while N^{3-} can be compensated with 3 Li^+ ions, a O ion substitution stabilizes a Li ion vacancy. There are two inequivalent N sites leading to two inequivalent O ion substitutions. Fig. 6(b) illustrates the "Left O" geometry in which the substituted N site has Wyckoff label *e* and Fig. 6(d) illustrates the "Right O" geometry in which the substituted N site has Wyckoff label *i*. The corresponding NEB diagrams for Li ion migration along the nearby $i \rightarrow e \rightarrow i \rightarrow e \rightarrow i$ paths are shown in Fig. 6(c). The energy diagram plots for the two substitution models are very similar (but not identical) and show that the presence of an O ion substitution does increase the migration energy barriers to $E_m \approx 0.5$ eV. Since the activation energy for conductivity in the presence of a native population of vacancies is $E_A = E_m$, the simulations support the notion that experimental samples of Li_7PN_4 may have O ion defects which stabilize Li ion vacancies and which increase the ionic conductivity.

In addition, we have investigated several possible Li ion interstitial mechanisms using the *I* and *II* type interstitial sites listed in Table 5. However, no direct hop or kickout paths were identified, based on geometric considerations.

3.2.3. Li_7PN_4/Li interfaces

A plausible cleavage plane for forming a surface of Li_7PN_4 is normal to a cube axis and exposes the smallest number of voids between PN_4 groups as shown in Fig. 7. We studied this (100) surface with a variety of Li configurations. The relaxed structures of two these interfaces is shown in Fig. 7. The structure shown in Fig. 7(a) is a highly symmetric structure, while the structure shown in Fig. 7(b) is less symmetric, but has an energy of 6.1 eV lower in the 192 atom simulation cell. The interface energy for configuration 7(b) (not corrected for strain) was found to be 0.04 eV/Å^2, a value similar to other LiPON/Li interfaces discussed above. The partial density of states for structure 7(b) is shown in Fig. 7(c). The corresponding partial densities of states for structure 7(a) is qualitatively similar, differing mostly in the partial densities of states contributions from metallic Li. The partial densities of states results shown in Fig. 7(c) indicates that this Li_7PN_4/Li system has the properties of an ideal interface. It is structurally metastable and the Fermi level of the system falls well within the band gap of the interior portion of the electrolyte so that it is expected that the system will be electrically insulating. It is interesting to note that $\langle N^a(E)\rangle$ curves corresponding to the interface region involving the P, N, and Li ions closest to the interface boundary, show small contributions within the band gap of bulk electrolyte, as shown in the middle planel of Fig. 7(c). The $\langle N^a(E)\rangle$ contribution for metallic Li shown in the top of Fig. 7(c) has the typical shape of that of a free-electron metal.

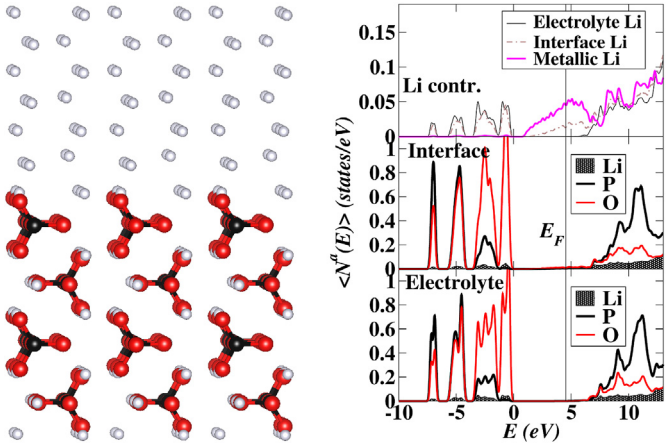

Fig. 8. Panel (a) shows ball and stick diagram of idealized γ-Li_3PO_4/Li with the surface normal oriented along the **b** axis shown in the vertical direction and the **a** axis of the electrolyte shown in the horizontal direction. The ball conventions are light gray, black, and red, representing Li, P, and O sites, respectively. Panel (b) shows the corresponding Partial densities of states plots for this interface, with separate $\langle N^a(E)\rangle$ contributions for the interior of the electrolyte, the interface region, and the contributions from the three types of Li sites using an expanded intensity scale. The zero of energy for the plots is taken as the top of the valence band of the bulk electrolyte. (For interpretation of the references to colour in this figure legend, the reader is referred to the web version of this article.)

Table 6
Comparison of calculated and measured activation energies. All energies are given in eV units.

Material	Mechanism	Simulation			Experiment
		E_f	E_m	$E_m+\frac{1}{2}E_f$	E_A
$Li_{14}P_2O_3N_6$	Vacancy	0.3	0.3	0.4	
$Li_{14}P_2O_3N_6$	Kickout	0.3	0.6	0.8	
Li_7PN_4	Vacancy	1.9	0.3	1.3	0.48[a]
Li_7PN_4 with O	Vacancy	––	0.5	––	
β-Li_3PO_4	Kickout	2.1[b]	0.4[b]	1.5[b]	
γ-Li_3PO_4	Kickout	1.7[b]	0.3[b]	1.2[b]	1.1–1.2[c]

[a] Ref. [15].
[b] Ref. [17].
[c] Ref. [42].

4. Summary and conclusions

The results of the reported simulations suggest that both nitrogen rich crystalline lithium oxonitridophosphate materials of this study – $Li_{14}P_2O_3N_6$ and Li_7PN_4 – show promising properties as solid electrolytes for Li ion batteries, possibly for use with Li metal anodes.

Simulations of idealized interfaces constructed for $Li_{14}P_2O_3N_6$/Li and Li_7PN_4/Li are structurally metastable and electrically insulating. In both of these cases, the partial densities of states associated with the interfaces show small effects in their electronic structures, while the partial densities of states associated with the interior of the electrolytes are identical to their bulk values. The partial densities of states associated with the metallic Li layers show that the Fermi level of the system lies well within the band gap of the interior layers of the electrolyte. An analogous study of idealized interfaces for γ-Li_3PO_4[**b**]/Li previously studied by Lepley et al. [21] is shown in Fig. 8(a) and (b). Here we see that the partial densities of states in the interface are somewhat less effected than in the case of the nitrogen rich electrolytes, while the partial densities of states associated with the interior of the electrolytes are identical to their bulk values. The partial densities of states associated with the metallic Li layers show that the Fermi level of the system lies well within the band gap of the interior layers of the electrolyte. Interestingly, the bottom of the metallic Li band in γ-Li_3PO_4[**b**]/Li lies above the top of the valence band of the electrolyte, while for the nitrogen-rich materials, the bottom of the metallic Li band lies approximately 1 eV below the top of the valence band of the electrolyte. While the total energy results for these LiPON electrolytes suggest exothermic reactions with Li under equilibrium conditions such as shown in Eqs. (6) and (8), these simulations show that LiPON/Li interfaces are likely to be practically stable as has been shown in experimental demonstrations [41].

The simulations also suggest that the activation energies for Li ion migration in the nitrogen rich electrolytes are also quite promising. Table 6 summarizes the simulation estimates of Li ion activation energies with experiment and with previous results for other isolated oxonitridophosphate materials. Here we see that the most efficient predicted activation energy for Li ion migration in $Li_{14}P_2O_3N_6$ is 0.3–0.4 eV for a pure vacancy mechanism involving g' site Li ions. The predicted activation energy for Li ion migration in $Li_{14}P_2O_3N_6$ is lower than the experimentally measured values for Li_7PN_4 [15] and for γ-Li_3PO_4 [42] as well as the $E_A = 0.6$ eV values measured for typical amorphous LiPON films [3]. The predicted activation energy of $E_A = 0.5$ eV for Li ion migration in Li_7PN_4 with Li ion vacancies, stabilized by O^{2-} ions substituting for N^{3-}, is close to that reported in experimental conductivity measurements for Li_7PN_4 [15]. It is also interesting to note that while for these nitrogen rich crystalline electrolytes, Li ion migration is dominated by vacancy mechanisms, while for Li_3PO_4 it was found that kickout mechanisms provide the most efficient ion migration processes [17]. While the simulations represent many competing factors which contribute to these results, it is perhaps reasonable to suggest a more general trend from the fact that each N^{3-} ion is associated with three Li ions while each O^{3-} ion is associated with two Li ions. It is therefore reasonable to expect that Li ion migration in structures with greater numbers of occupied Li sites are likely to occur via vacancy mechanisms while structures with smaller numbers of occupied Li sites are likely to occur via mechanisms having more active involvement of the interstitial sites.

Acknowledgements

This work was supported by NSF grant DMR-1507942. Computations were performed on the Wake Forest University DEAC cluster, a centrally managed resource with support provided in part by the University. We would also like to thank Dr. Nicholas Lepley for the use of his unpublished simulations of a γ-Li_3PO_4/Li interface.

References

[1] N.J. Dudney, Thin film micro-batteries, Interface 17 (3) (2008) 44–48 (3).
[2] J.B. Bates, N.J. Dudney, B. Neudecker, A. Ueda, C.D. Evans, Thin-film lithium and lithium-ion batteries, Solid State Ionics 135 (2000) 33–45.
[3] X. Yu, J.B. Bates, J.G.E. Jellison, F.X. Hart, A stable thin-film lithium electrolyte: lithium phosphorus oxynitride, J. Electrochem. Soc. 144 (1997) 524–532.
[4] B. Wang, B.C. Chakoumakos, B.C. Sales, B.S. Kwak, J.B. Bates, Synthesis, crystal structure, and ionic conductivity of a polycrystalline lithium phosphorus oxynitride with the γ-Li_3PO_4 structure, J. Solid State Chem. 115 (1995) 313–323.
[5] J.B. Bates, N.J. Dudney, D.C. Lubben, G.R. Gruzalski, B.S. Kwak, X. Yu, R.A. Zuhr, Thin-film rechargeable lithium batteries, J. Power Sources 54 (1995) 58–62.
[6] B. Wang, B.S. Kwak, B.C. Sales, J.B. Bates, Ionic conductivities and structure of lithium phosphorus oxynitride glasses, J. Non-Crystalline Solids 183 (1995) 297–306.
[7] J.B. Bates, G.R. Gruzalski, N.J. Dudney, C.F. Luck, X. Yu, Rechargeable thin-film lithium batteries, Solid State Ionics 70–71 (1994) 619–628.
[8] J.B. Bates, N.J. Dudney, G.R. Gruzalski, R.A. Zuhr, A. Choudhury, D.F. Luck, J.D. Robertson, Fabrication and characterization of amorphous lithium electrolyte thin films and rechargeable thin-film batteries, J. Power Sources 43–44 (1993) 103–110.
[9] J.B. Bates, N.J. Dudney, G.R. Gruzalski, R.A. Zuhr, A. Choudhury, D.F. Luck, J.D. Robertson, Electrical properties of amorphous lithium electrolyte thin films, Solid State Ionics 53–56 (1992) 647–654.
[10] Y.A. Du, N.A.W. Holzwarth, First-principles study of LiPON and related solid electrolytes, Phys. Rev. B 81 (2010) 184106 (15pp).
[11] K. Senevirathne, C.S. Day, M.D. Gross, A. Lachgar, N.A.W. Holzwarth, A new crystalline LiPON electrolyte: synthesis, properties, and electronic structure, Solid State Ionics 333 (2013) 95–101.
[12] E.-M. Bertschler, C. Dietrich, J. Janek, W. Schnick, $Li_{18}P_6N_{16}$ - a lithium nitridophosphate with unprecedented tricyclic $[P_6N_{16}]_{18-}$ ions, Chem. A Eur. J. 23 (2017) 2185–2191.
[13] D. Baumann, W. Schnick, $Li_{14}(PON_3)_2O$ - a non-condensed oxonitridophosphate oxide, Eur. J. Inorg. Chem. 2015 (4) (2015) 617–621.
[14] W. Schnick, J. Luecke, Synthesis and crystal structure of lithium phosphorus nitride Li_7PN_4: the first compound containing isolated PN_4 tetrahedra, J. Solid State Chem. 37 (1990) 101–106.
[15] W. Schnick, J. Luecke, Lithium ion conductivity of $LiPN_2$ and Li_7PN_4, Solid State Ionics 38 (1990) 271–273.

[16] Y.A. Du, N.A.W. Holzwarth, Li ion diffusion mechanisms in the crystalline electrolyte γ-Li_3PO_4, J. Electrochem. Soc. 154 (2007) A999–A1004.
[17] Y.A. Du, N.A.W. Holzwarth, Mechanisms of Li^+ diffusion in crystalline Li_3PO_4 electrolytes from first principles, Phys. Rev. B 76 (2007) 174302 (14 pp).
[18] Y.A. Du, N.A.W. Holzwarth, Effects of O vacancies and N or Si substitutions on Li^+ migration in Li_3PO_4 electrolytes from first principles, Phys. Rev. B 78 (2008) 174301.
[19] N.A.W. Holzwarth, N.D. Lepley, Y.A. Du, Computer modeling of lithium phosphate and thiophosphate electrolyte materials, J. Power Sources 196 (2011) 6870–6876.
[20] N.D. Lepley, N.A.W. Holzwarth, Y.A. Du, Structures, Li+ mobilities, and interfacial properties of solid electrolytes Li_3PS_4 and Li_3PO_4 from first principles, Phys. Rev. B 88 (2013) 104103 (11 pp).
[21] N.D. Lepley, N.A.W. Holzwarth, Modeling interfaces between solids: application to Li battery materials, Phys. Rev. B 92 (2015) 214201.
[22] P. Hohenberg, W. Kohn, Inhomogeneous electron gas, Phys. Rev. 136 (1964) B864–B871.
[23] W. Kohn, L.J. Sham, Self-consistent equations including exchange and correlation effects, Phys. Rev. 140 (1965) A1133–A1138.
[24] P.E. Blöchl, Projector augmented-wave method, Phys. Rev. B 50 (1994) 17953–17979.
[25] N.A.W. Holzwarth, A.R. Tackett, G.E. Matthews, A Projector Augmented Wave (PAW) code for electronic structure calculations, Part I: *atompaw* for generating atom-centered functions, Comput. Phys. Commun. 135 (2001) 329–347 available from the website http://pwpaw.wfu.edu.
[26] P. Giannozzi, S. Baroni, N. Bonini, M. Calandra, R. Car, C. Cavazzoni, D. Ceresoli, G.L. Chiarotti, M. Cococcioni, I. Dabo, A.D. Corso, S. de Gironcoli, S. Fabris, G. Fratesi, R. Gebauer, U. Gerstmann, C. Gougoussis, A. Kokalj, M. Lazzeri, L. Martin-Samos, N. Marzari, F. Mauri, R. Mazzarello, S. Paolini, A. Pasquarello, L. Paulatto, C. Sbraccia, S. Scandolo, G. Sclauzero, A.P. Seitsonen, A. Smogunov, P. Umari, R.M. Wentzcovitch, Quantum espresso: a modular and open-source software project for quantum simulations of materials, J. Phys. Condens. Matter 21 (39) (2009) 394402 (19pp), available from the website, http://www.quantum-espresso.org.
[27] A. Kokalj, XCrySDen– an new program for displaying crystalline structures and densities, J. Mol. Graph. Model. 17 (1999) 176–179 code available at the website, http://www.xcrysden.org.
[28] A. Kokalj, Computer graphics and graphical user interfaces as tools in simulations of matter at the atomic scale, Comput. Mater. Sci. 28 (2003) 155–168.
[29] K. Momma, F. Izumi, Vesta 3 for three-dimensional visualization of crystal, volumetric, an morphology data, Appl. Crystallogr. 44 (2011) 1272–1276 code available from the website, http://jp-minerals.org/vesta/en/.
[30] J.P. Perdew, Y. Wang, Accurate and simple analytic representation of the electron-gas correlation energy, Phys. Rev. B 45 (1992) 13244–13249.
[31] N.D. Lepley, N.A.W. Holzwarth, Computer modeling of crystalline electrolytes – lithium thiophosphates and phosphates, J. Electrochem. Soc. 159 (2012) A538–A547.
[32] Z.D. Hood, C. Kates, M. Kirkham, S. Adhikari, C. Liang, N.A.W. Holzwarth, Structural and electrolyte properties of $Li_4P_2S_6$, Solid State Ionics 284 (2015) 61–70.
[33] H. Jónsson, G. Mills, K.W. Jacobsen, Nudged elastic band method for finding minimum energy paths of transitions, in: B.J. Berne, G. Ciccotti, D.F. Coker (Eds.), Classical and Quantum Dynamics in Condensed Phase Simulations, World Scientific, Singapore, 1998, pp. 385–404.
[34] G. Henkelman, B.P. Uberuaga, H. Jónsson, A climbing image nudged elastic band method for finding saddle points and minimum energy paths, J. Chem. Phys. 113 (2000) 9901–9904.
[35] G. Henkelman, H. Jónsson, Improved tangent estimate in the nudged elastic band method for finding minimum energy paths and saddle points, J. Chem. Phys. 113 (2000) 9978–9985.
[36] A.R. West, Basic Solid State Chemistry, second ed., John Wiley & Sons, LTD, 1999.
[37] T. Hahn (Ed.), International Tables for Crystallography, Volume a: Space-group Symmetry, Fifth Revised Edition, Kluwer, 2002. ISBN 0-7923-6590-9. The symmetry labels used in this work are all based on this reference.
[38] A. Al-Qawasmeh, J. Howard, N.A.W. Holzwarth, Li_4SnS_4 and Li_4SnSe_4: simluations of their structure and electrolyte properties, J. Electrochem. Soc. 164 (2017) A6386–A6394.
[39] Y.A. Du, N.A.W. Holzwarth, Li ion migration in Li_3PO_4 electrolytes: effects of O vacancies and N substitutions, ECS Trans. 13 (2008) 75–82.
[40] S.P. Ong, L. Wang, B. Kang, G. Ceder, $LiFePO_2$ phase diagram from first principles calculations, Chem. Mater. 20 (5) (2008) 1798–1807.
[41] J. Li, C. Ma, M. Chi, C. Liang, N.J. Dudney, Solid electrolyte: the key for high-voltage lithium batteries, Adv. Energy Mater. 5 (4) (2015) 1401408.
[42] A.K. Ivanov-Shitz, V.V. Kireev, O.K. Mel'nikov, L.N. Demainets, Growth and ionic conductivity of γ-Li_3PO_4, Crystallogr. Rep. 46 (2001) 864–867.